Leaf Bidirectional Transmittance Distribution Function Estimates and Models for Select Deciduous Tree Species

Benjamin D. Roth, *Member, IEEE*, M. Grady Saunders, Charles M. Bachmann, *Senior Member, IEEE*, and Jan van Aardt, *Member, IEEE*

Abstract—Remote sensing increasingly has become an important tool for forest management. In the development of forest metrics from remote-sensing data, currently many models omit the individual leaf bidirectional scattering distribution function (BSDF). Past studies, and the currently available data, often do not adequately incorporate transmission, cover the broader reflective domain, and/or incorporate models to extend to any illumination and view angle combination. We estimated broadleaf bidirectional transmittance distribution functions (BTDFs) in this study using the goniometer of the Rochester Institute of Technology-Two (GRIT-T), which records spectral data in the UV-A through shortwave infrared (SWIR) spectral regions (350–2500 nm). We measured three species of large tree leaves, Norway maple (*Acer platanoides*), American sweetgum (*Liquidambar styraciflua*), and northern red oak (*Quercus rubra*). We accurately modeled leaf BTDF with extension to any illumination angle, viewing zenith, and azimuthal angle through nonlinear regression to a physically-based microfacet BTDF. The model fit showed a mean of less than 7% normalized root-mean-squared error (NRMSE) spectrally from 450 to 2300 nm (lower and upper wavelength range omitted due to detector noise). The microfacet models provide highly useful physical quantities such as a relative roughness, index of refraction, and absorption, which are all directly related to leaf optical properties. These physical quantities have implications for plant physiology, vegetation remote sensing, and physics-based image generation. Specifically, the accuracy of radiative transfer modeling in forest canopies depends on rigorous representations of leaves, and this increase in accuracy can lead to the development of higher fidelity data processing algorithms for remote sensing. Data and programing scripts are available at- http://dx.doi.org/10.21227/yjek-2059

Index Terms—Bidirectional scattering distribution function (BSDF), bidirectional transmittance distribution function (BTDF), goniometer, hyperspectral, leaf optical properties, remote sensing, spectroradiometer.

I. INTRODUCTION

CHARACTERIZATION of leaf anisotropic scattering has implications for plant physiology, vegetation remote sensing, and physics-based image generation. In most remote-sensing simulations, past work has assumed leaves in a plant canopy followed a Lambertian assumption or alternatively used generic bidirectional scattering distribution function (BSDF) models. However, we believe leaf-level BSDF measurements and estimates are necessary for fully understanding light transport in canopies. Such measurements would enable scaling from leaf- to canopy-level, or to even regional-level, all the while ensuring high fidelity in the scaling of leaf optical properties.

The BSDF comprises both the bidirectional reflectance distribution function (BRDF) [1]–[3] and the bidirectional transmittance distribution function (BTDF) [4], [5]. Because the BSDF is based on infinitesimals, it cannot be directly measured [1]. Instead, we measure the biconical reflectance factor (BCRF) and biconical transmittance factor (BCTF). The BCRF is an estimate of the bidirectional reflectance factor (BRF), where BRDF $= \frac{\text{BRF}}{\pi}$, with the same relationship holding true for the BCTF and bidirectional transmittance function (BTF). Therefore, any reference to BRDF or BTDF measurements, in this or other publications, is in fact an estimate from the BCRF or BTDF respectively [1], [2]. Previous research and publicly-available single-leaf BSDF data are extremely limited, even though the importance of leaf-level scattering properties are well known.

Recently, we developed a broad leaf BSDF database [6] composed of both leaf BRDF [7] and the leaf BTDF, which is the focus of the study presented here. Prior to the development of the broad leaf BSDF database, the Institut de Physique du Globe de Paris, Paris, France, maintained the only known leaf-level BSDF data. Their database includes seven species and nine total samples, based solely on BRDF measurements [8]. That database comprises data for leaf-level BRDF characterizations used by Bousquet *et al.* [9], who examined the spectral and directional variations of leaf BRDF by making measurements of three leaf types: laurel, European beech, and hazel, for wavelengths between 480 and 880 nm, at 1-nm intervals. Their spectral modeling used a summation of both a specular and a diffuse component along with a least-squares nonlinear minimization. Their fit to the specular component used a Cook and Torrance [10] microfacet, physically-based model, while their fit of the diffuse component used a simple Lambert coefficient. Their results exhibited limited variance of the specular component throughout the

visible and near-infrared wavelengths, while producing significant anisotropic scattering in the chlorophyll absorption regions of the spectra. Biliouris *et al.* [11] also made leaf BCRF measurements, but examined statistical properties of within-species variation from 60 European beech tree leaves over the spectral range of 400–2500 nm. A quantile–quantile study showed that the leaves belonged to the same distribution and population. Their BRDF modeling incorporated the semiempirical Rahman–Pinty–Verstraete (RPV) model [12]. Their approach required a different set of parameters for each illumination angle, and the poor generalization to other illumination angles was attributed to the fact that the RPV model was designed as a canopy-level, heterogeneous model.

Compared with BRDF analyses, leaf-level BTDF studies are far more scarce, as studies have typically assumed that the contribution of directional transmission to remote-sensing data is minimal [13], [14], and the experimental setup requires greater complexity [15]. Walter-Shea [16] completed one of the first studies on directional scattering from leaves that included BTDF. This study specifically examined corn and soybean BSDF, and although the BTDF data were largely diffuse in the visible spectrum, the soybean measurements exhibited distinct maxima that were particularly pronounced at nadir illumination. That study was limited in spectral resolution using only two broadband sensors: one in the visible and the other in the near-infrared spectral domain. Brakke *et al.* [17] and Brakke [18] similarly noted a maximum for nadir illumination and observation when characterizing leaf BTDF. In their study, they characterized only the principle plane of oak and maple leaves at the single wavelength of 632.8 nm using a helium neon laser. Greiner *et al.* [19] also used a single-laser wavelength, 1064 nm, to estimate the principle plane leaf BSDF of sugar maple and eastern cottonwood trees. During their preliminary experiments, they found a correlation between leaf freshness and the scattering amplitudes, with dryer leaves being more reflective and less transmissive. They were able to fit their BTDF data with a second-order polynomial. Even though their study was highly detailed, they nevertheless normalized their models in such a way that would make it difficult to extract the actual BSDF. In turn, the study by Combes *et al.* [15] was able to capture leaf BTDF estimates beyond the principle plane with an in-house goniometer, dedicated to the study of leaf bidirectional optical properties. However, their study concentrated on leaf BRDF, only reported the BTDF estimates of a beech leaf and concluded that the BTDF is largely isotropic, with increased transmission along the principle plane.

Leaf-level directional transmittance arguably is of great consequence for certain remote-sensing data. This may particularly be true when modeling lidar in forest canopies, as leaf surfaces can be >50% transparent for lidar systems that operate at near-infrared wavelengths [20]. However, recent studies leveraging the new information in this work have shown negligible contribution for airborne lidar at 550, 1064, and 1550 nm [21]. Future research will address the generality of this result by considering other remote-sensing modalities and scales. For instance, remote-sensing systems that capture photosynthetically active radiation (PAR) from

beneath the canopy are also affected by leaf-level transmission scattering [22]. However, most remote-sensing simulations in vegetation canopies presume purely Lambertian transmission, or even worse, assume that leaves are opaque [13], [14], mainly due to the lack of leaf-level BTDF data. Previous studies have produced data limited in spectral extent, lacked models to characterize directional scattering at angles beyond those measured, and used methods that were not extensible to remote-sensing simulations. Consequently, the objectives of this study are to 1) develop a method for accurate leaf BCTF spectral measurements, from the visible through shortwave infrared (SWIR); 2) evaluate a BTDF model which fits measurements and generalizes to all possible illumination and view directions; and 3) analyze leaf BTDF features and differences between measured species.

This study therefore made high spectral resolution (350–2500 nm) measurements with the goniometer of the Rochester Institute of Technology-Two (GRIT-T) [23], [24], capturing directional transmission optical properties of three broadleaf tree species (Norway maple, American sweetgum, and northern red oak) [7]. Since GRIT-T previously had exclusively been used for reflectance measurements [23]–[28], we had to develop a new approach to collect transmission data. We then evaluated our measurements against past measurements in the literature. BSDF models were evaluated, and we ultimately developed a modeling technique that accurately fit the observed leaf BTDF measurements. Our single-scattering (specular) versus diffuse fraction analysis also explains at which wavelengths the directional transmission contribution is largest.

II. Measurement Methods

We used GRIT-T to capture leaf biconical spectral transmittance measurements from 350 to 2500 nm. GRIT-T provides automation capability and high precision that maintains the same spot on the target within 10 mm [23], [24]. Extensive use of GRIT-T has proven its capability in the laboratory and field environments [7], [24]–[28].

We collected and measured the BCTF of leaves from Norway maple (*Acer platanoides*), American Sweetgum (*Liquidambar styraciflua*), and northern red oak (*Quercus rubra*), trees in Rochester, NY, USA in August of 2019. For each species, we collected the leaf samples from the same tree, selecting larger leaves, which typically are thin sunlit leaves. Although these leaves may not be representative of all leaves in the canopy, the large surface area was needed to fill the field-of-view (FOV) of the goniometer while ensuring an adequate viewing margin. The three species had different observable features: the oak leaves exhibited a glossy epidermis and structural stiffness due to a thick cuticle layer, while the sweetgum leaves manifested a glossy surface and greater flexibility, and the maple leaves appeared matte and flexible, also being the thinnest. An example of the three leaf types are shown in Fig. 1.

After collection, leaf samples were immediately placed in airtight bags and stored at nominal refrigeration temperatures. We completed the measurements on the same day to minimize
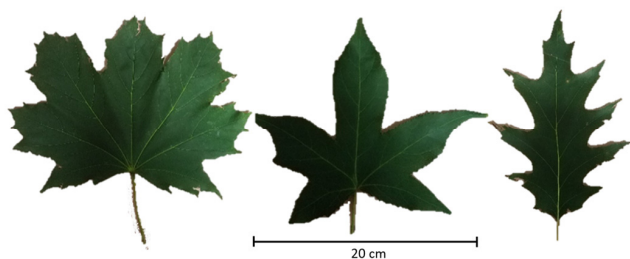
Fig. 1. Example images of leaves used in transmission measurements. (From left to right) Norway maple, American sweetgum, and northern red oak.
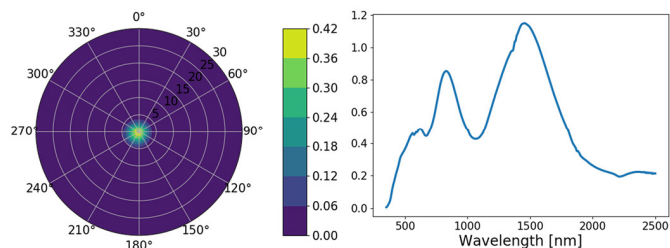

Fig. 2. Left polar plot displays the light source measurement at 1064 nm after interpolation. The right plot is the measured radiance spectrum of the Solux halogen lamp, with the neutral density filter at the 0° source position. Both plots are in spectral radiance units of $\left(\mathrm{W} \cdot \mathrm{cm}^{-2} \cdot \mathrm{sr}^{-1} \cdot \mathrm{nm}^{-1} \right)$.

leaf optical changes. Each measurement cycle consisted of a single illumination zenith angle, with the goniometer moving to 49 different observation angles along 15° zenith steps (0–60°), and 30° steps in azimuth (0–330°). The measurement cycle was repeated for each leaf type, with source zenith angles of 0°, 15°, 30°, and 45°, using a new leaf of the same species to minimize leaf drying effects. Scans along azimuth planes allowed for repeated nadir measurements to confirm consistency. We chose the specific scan density in an effort to minimize the scan time and thereby prevent leaf drying [19], while also capturing the transmittance directional structure. We maintained a 0.5 m distance between the sample and the goniometer. A 2.6-cm FOV at 0° zenith and a 5.2-cm FOV at 60° zenith angle resulted from using a 3° fore-optic. Though a statistical analysis through many repeated measurements was not accomplished due to the difficulty in making the measurements, some of the leaf-to-leaf variability was accounted for when modeling the BTDF by incorporating a new leaf at each source angle.

Transmission measurements proved to be complex, since GRIT-T had not previously been used in a transmission measurement configuration. A Solux halogen 50 W, 4700 K, 36° spread light was used as the illumination source, with a diffuser to ensure uniform illumination. To prevent saturation when capturing the directionality of the light source, we used a neutral density filter. To capture the source directionality, our measurements densely sampled in 2° in both zenith and azimuthal increments over a 20° cone, centered on the light source, along with sparser sampling using 20° zenith and 60° azimuthal increments. To interpolate these measurements, we first projected the light-source measured radiance values onto a two-dimensional polar projection and then performed a cubic interpolation over a 1° grid of azimuth and zenith angles. The interpolated polar plot and source spectra appear in Fig. 2. As seen in the interpolated polar plot, the light source spread was less than 5°.

Preliminary experiments to collect transmission data resulted in anomalous artifacts due to the light source distance, stray light, leaf freshness, and insufficient filling of the FOV of the sensor. The preliminary experiments dictated the setup that was used in this study. A "light box" was created that housed the light source with an attached 7.6-cm-diameter pipe on a hinge to appropriately direct the light. To achieve alignment of the source at the four illumination directions, we moved the light source and oriented it within the light box, while ensuring that the sample remained level. We placed a disk
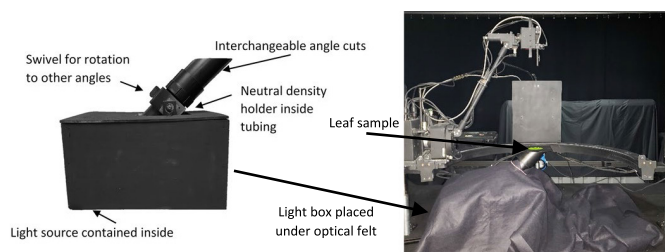

Fig. 3. (Left figure) Light box apparatus with labeled components. (Right image) Experimental setup with GRIT-T. The laboratory is configured with absorbing material and isolated from external illumination in order to prevent stray light.

with a 5 cm aperture near the entry of the pipe to serve as a holder for a neutral density filter, which we used to prevent saturation during direct light source characterizations. The disk also reduced stray reflections off the sides of the light-directing tubing. We also covered the apparatus with optical black felt to prevent stray light. The sample rested on top of the tubing about 40 cm above the light source (for the nadir configuration). We placed each leaf in a sample holder that served to flatten the leaf at the edges while also ensuring the leaf filled the sensor FOV. The effect was to minimize large undulations and asymmetries, while keeping the microstructure intact. We covered the inside surface of the tubing and the sample holder with flat black "high heat" paint, and to assess residual stray light reflecting off the interior sides of the tubing, we collected spectrometer measurements. All assessments showed less than one tenth of a percent of spectral reflectance off the sides of the tubing, across all wavelengths (350–2500 nm). We then made transmission measurements with the light source at 0°, 15°, 30°, and 45° from zenith under the leaf, while GRIT-T measured the transmitted light from above. To achieve the preferred distance to the sample, we placed GRIT-T on raising struts. The leaf was placed each time with the stem along the principle plane, consisting of the illumination and leaf normal vectors. The full experimental setup appears in Fig. 3.

We calculated the leaf BCTF by dividing the goniometer radiance values at a particular azimuth and zenith by the radiance value that would result from a lossless perfect diffuser

$$\mathrm{BCTF} = \frac{L(\theta, \phi)_{\mathrm{sample}}}{L_{\mathrm{diff\_lossless}}}. \tag{1}$$

We determined the radiance of a lossless perfect diffuser for a given light source configuration using measurements of a broadband hybrid diffuser (diffuse plate) [29], with the same scan pattern as the leaves. Integrating over the radiance measurements from the diffuser and dividing over the Lambertian solid angle, π, yield the perfectly diffuse radiance

$$L_{\text{diff}} = \frac{\int_0^{2\pi} \int_0^{\pi} L(\theta, \phi) \sin(\theta) d\theta d\phi}{\int_0^{2\pi} \int_0^{\pi} \sin(\theta)\cos(\theta) d\theta d\phi = \pi} \qquad (2)$$

where L_{diff} is the perfectly diffuse radiance and $L(\theta, \phi)$ represents the measured radiance values. We performed the integration over interpolated radiance values at one-degree azimuth, $\Delta\phi$, and zenith, $\Delta\theta$, intervals. For notational brevity, even though the radiance values are also all wavelength dependent, they do not appear explicitly in the equations. We filled in angles beyond those measured with nearest neighbor interpolation. In order to find the lossless perfectly diffuse radiance (no absorption or reflection), we then divide L_{diff} by the directional hemispherical transmittance (DHT) of the plate

$$L_{\text{diff\_lossless}} = \frac{L_{\text{diff}}}{\text{DHT}_{\text{plate}}}. \qquad (3)$$

We computed $\text{DHT}_{\text{plate}}$ by characterizing the DHT with a 0.5-m-diameter integrating sphere, thereby taking advantage of étendue reciprocity between the hemispherical source and the direction of observation [30]. A plasma and halogen source illuminated the integrating sphere through ports. One ASD FieldSpec 4 Hi-Res spectroradiometer, with bare fiber, measured the internal radiance of the sphere, while a second was placed outside the sphere, collecting spectral data through the port-hole at a distance of 20 cm, with a 5° fore-optic. The diffuse plate then was placed directly on the porthole. We made measurements at 0°, 15°, 30°, and 45° look angles. We also made measurements without the plate in place (external sensor recorded spectral radiances ~5% higher than the internal sensor) in order to normalize the two sensors to each other and reduce noise. Then, we determined DHT by dividing the spectral radiance from the external sensor by the spectral radiance from the internal sensor. When the sensor normalization was applied, the DHT slightly dropped in amplitude and the data were considerably smoothed. Five sets of measurements taken at each of the four viewing angles showed insignificant variation. We averaged each of the five measurements to produce a curve for a particular viewing angle and then computed the mean of the four viewing angles to produce a single transmittance curve to be used in calculations. Artifacts observed in the water absorption region between 1850 and 2300 nm likely stem from backscatter from the plate back into the sphere. Backscattered light has a longer path length and more attenuation results in parts of the spectrum affected by water absorption. Therefore, we used linear interpolation between 1850 and 2300 nm to produce the final DHT of the plate. Due to minimal observed variance between look angles, we were able to use the same curve for the DHT at each illumination angle when computing leaf transmittance. We also computed $\text{DHT}_{\text{plate}}$ by dividing L_{diff} by $L_{\text{diff}_{\text{light}}}$, using the $L_{\text{diff}_{\text{light}}}$ calculated in (2), but from direct
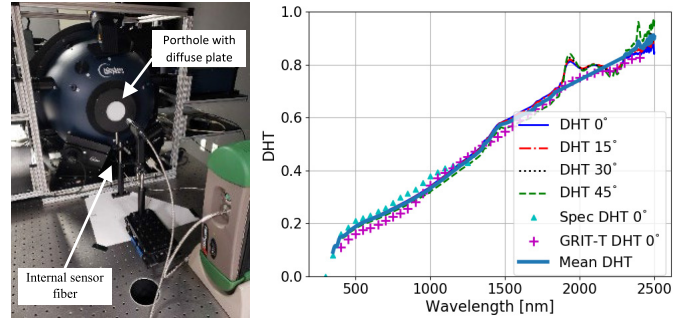

Fig. 4. (Left image) Experimental setup of the integrating sphere with the external spectroradiometer. The fiber for the internal sensor is also seen coming out of the bottom of the sphere, and the diffuse plate is mounted against the porthole. (Right plot) $\text{DHT}_{\text{plate}}$ calculated for each view angle, the vendor calibration from Edmund Optics [29] at nadir, and the transmission calculated when using GRIT-T at nadir illumination.

measurements of the light source (small diffuser plate directly over bulb). This only worked for nadir illumination because at off-nadir angles, the light source distance is greater and the small diffuser directly in front of the light did not fill the sensor FOV. An image of the experimental setup and a plot of the calculated DHT appear in Fig. 4. The transmission curves calculated from the integrating sphere data at all view angles (0–45°) in the plate transmission plot lie between the vendor calibration (only measured out to 1250 nm) and the nadir GRIT-T measurement. We ultimately used the curve labeled "Mean DHT," i.e., the mean of all the view angles from the integrating sphere as the DHT for leaf BCTF calculations.

The BCTF calculation tends to amplify noise in parts of the spectrum where the signal is low. We therefore applied a 10-nm moving average filter via 1-d kernel convolution to reduce noise. We observed very few outliers since we had taken extra precautions in aligning the experimental setup while ensuring the sample filled the sensor FOV. We identified and removed a few existing outliers in the data below the 25th percentile interquartile range (IQR) [31].

III. MEASUREMENT RESULTS

For each leaf type and source zenith angle, Fig. 5 presents overlaid spectral plots recorded for each observation vector. Fig. 5 allows for a top-level understanding of the BCTF measurements across the spectrum with the magnitudes representing the overall transmittance and the spread between spectral lines representing a larger specular component. Fig. 5 shows a general trend, where thicker leaf cuticle correlates with more diffuse leaf BCTF (less spread between the spectral lines at different sensor viewing angles). Also, as the illumination zenith angle increases, the leaf also becomes more diffuse. The only exception to this is the sweetgum at 45° illumination angle, likely due to leaf-to-leaf variability.

In Fig. 5, noise is visible at both ends of the spectrum, and is most apparent above 2000 nm. The requirement of shorter sampling times to reduce the effects of leaf drying increased this noise level. For these reduced integration times, further investigation highlighted low signal-to-noise ratios (SNRs), i.e., less than 10, for wavelengths below 450 nm and

This article has been accepted for inclusion in a future issue of this journal. Content is final as presented, with the exception of pagination.

ROTH *et al.*: LEAF BTDF ESTIMATES AND MODELS FOR SELECT DECIDUOUS TREE SPECIES 5
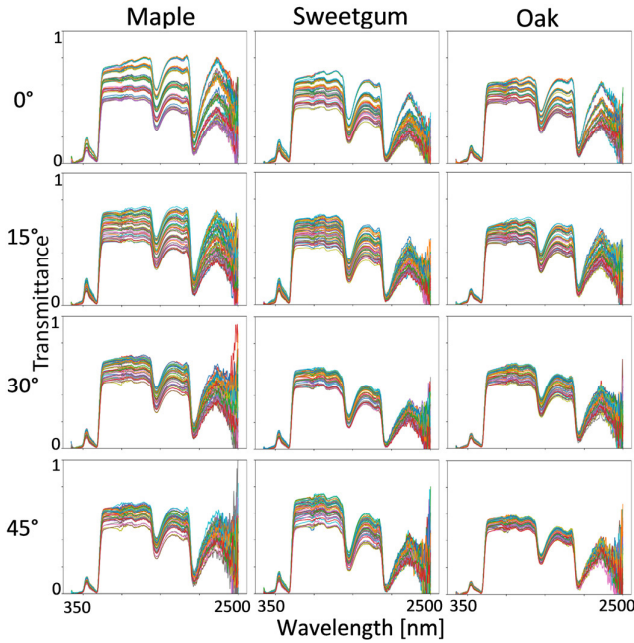

Fig. 5. Spectral transmittance plots (350–2500 nm) with each of the measurements of the 49 sensor locations overlaid for each leaf type (maple, sweetgum, and oak) at each source zenith angle (0°, 15°, 30°, and 45°).

above 2000 nm, while the remaining spectrum exhibited SNRs greater than 500. Under the assumption that the signal will vary slowly over this interval (excluding known vegetation features, e.g., red edge) [7], we computed the mean and standard deviation of the SNR using a 10-nm sliding window.

To assess measurement accuracy, we made a qualitative comparison of the DHT to previous studies of the same leaf type. To obtain the DHT, we integrated the estimated BTDF, $f_t(\theta_i, \phi_i; \theta_o, \phi_o)$, with θ_i and ϕ_i source zenith and azimuthal angles and θ_o and ϕ_o observation source zenith and azimuthal angles over the hemisphere, following the method presented by Schaepman-Strub *et al.* [2]:

$$\text{DHT}(\theta_i, \phi_i, \lambda)$$
$$= \int_0^{2\pi} \int_0^{\frac{\pi}{2}} f_t(\theta_i, \phi_i; \theta_o, \phi_o) \cos(\theta_o) \sin(\theta_o) d\theta_o d\phi_o. \quad (4)$$

We performed the integration on a grid comprised of cubic interpolated points from a polar projection of the measurements and extended the results beyond measured zenith values through nearest neighbor interpolation. Our method shows good agreement with prior measurements as seen in Fig. 6.

The differences seen in our maple DHT plot compared with that of Hovi *et al.* [32] are due to variances in the measurement method and the leaves. The lower signal in the visible is a result of our use of thin, matured sunlit leaves, which are typically darker in the visible due to increased chlorophyll absorption [33], [34]. We also see a difference in the water absorption bands, attributed to the advanced seasonal stage. The measurements also take about 12 min to collect, with some amount of leaf drying expected over this period. The published integrating sphere measurements performed by Hovi *et al.* [32] can be made in a fraction of this time.
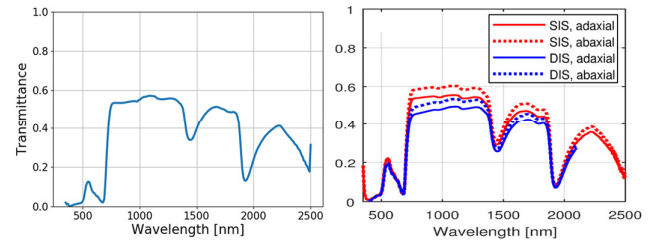

Fig. 6. (Left plot) Our calculated DHT for adaxial side of a Norway maple leaf, with a nadir source. (Right plot) Norway maple leaf DHT presented by Hovi *et al.* [32]. Legend labels: SIS is measured with a single integrating sphere, and DIS is measured with a double integrating sphere. (Figure adapted with permission of the author, copyright holder).

Another validation exercise is to compare results to previously published leaf-level data. Combes *et al.* [15], who described the capability of the spectrogoniophotometer located at the Institut de Physique du Globe de Paris (Fig. 7), have published the only full leaf BTDF known to the authors, i.e., beyond the principle plane. Though their leaf species were different, their overall scale was nearly identical to ours, and we observe similar behavior between the beech leaf measured by Combes *et al.* [15] and the maple leaf in this study. For the specular peak, Fig. 7 shows a general trend of decreasing amplitude with increasing illumination zenith angle. The overall shape of the BTDF can be characterized as having a constant wavelength-dependent diffuse background component, as well as a more directional specular component. The specular peak at 660 nm is offset from the principal plane and opposite to the direction of illumination, as expected, but tends to remain in place after its original offset with increasing illumination zenith angle. Comparison of the BTDF at a high absorption wavelength (660 nm) to a high transmittance wavelength (1060 nm) shows that the overall BTDF shape is largely conserved for each illumination zenith angle. The BTDF at 1064 nm is greater due to a bias caused by the large diffuse background component and an increase in scale of the specular component due to higher transmittance.

A comparison of the leaf directional transmittance of the three leaf species for three wavelengths (550, 1060, and 1550 nm) appears in Fig. 8 for a 15° illumination zenith angle. The maple leaf is the thinnest and most transparent of the three leaves, thus transmitting the most light, as well as exhibiting the most directional light for all three wavelengths. At 550 nm, the sweetgum leaf is slightly more diffuse, and the oak clearly is the most diffuse with the least transmittance. This behavior is due to the thicker cuticle layer of the oak, and glossier surface of the sweetgum leaf, when compared with the maple. At 1060 nm, the internal leaf structures absorb minimal light, thus causing a much higher diffuse and directional component for each of the three leaf types [18]. The oak and sweetgum leaves still exhibit less transmission and are more diffuse than the maple, but now have similar scales to each other. At 1550 nm, the sweetgum leaf has a much stronger water absorption component, causing less transmittance that is more diffuse.

IV. MODELING METHODS

In order to accomplish our objective to generalize the BTDF to any source and view angle, we investigated several different

This article has been accepted for inclusion in a future issue of this journal. Content is final as presented, with the exception of pagination.

6

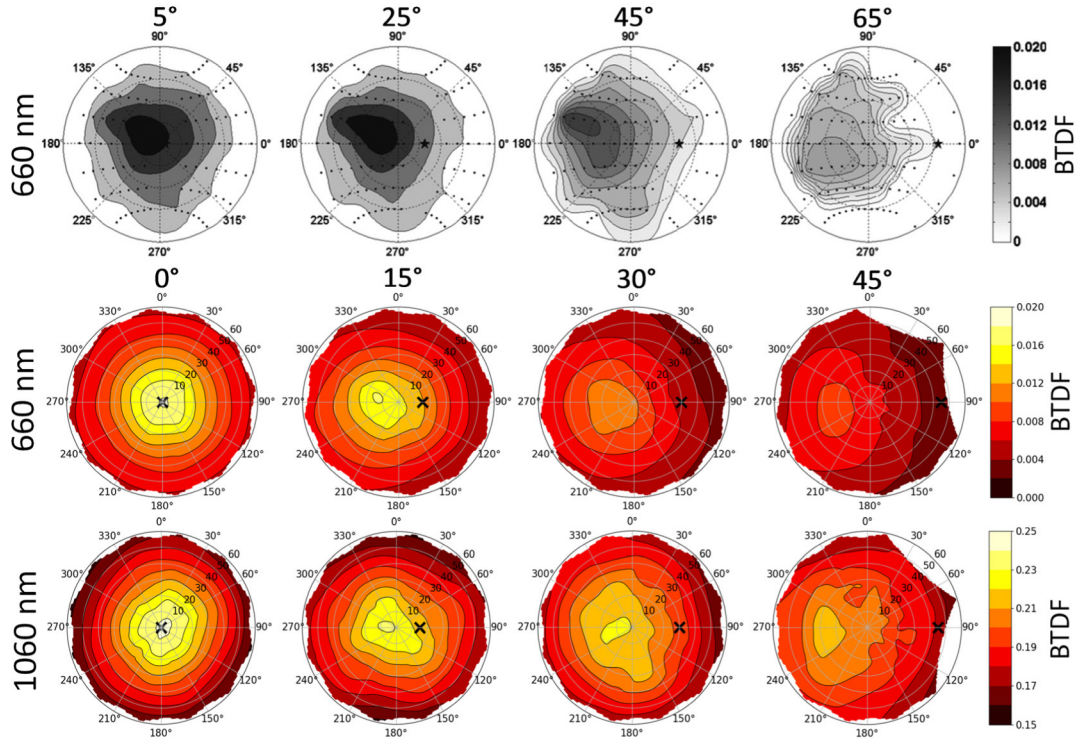IEEE TRANSACTIONS ON GEOSCIENCE AND REMOTE SENSING

Fig. 7. (Top row) Previously-published BTDF of a beech leaf at 660-nm wavelength [15] (figure adapted with copyright permissions). (From left to right) Illumination source is located at zenith angle of 5°, 25°, 45°, and 65°. The axial rings are in 20° increments, the dots mark measurement locations, and the star indicates the illumination direction. (Middle and bottom rows) Measurements from this study on the maple leaf at wavelengths 660 and 1060 nm, respectively. (From left to right) Illumination angles are marked by a black X at 0°, 15°, 30°, and 45°, while the axial rings are in 10° increments. White space within the polar plot signifies either no data or omitted outlier data. Notice the scale of the BTDF at 660 nm is nearly identical to those previously published by Combes *et al.* [15].
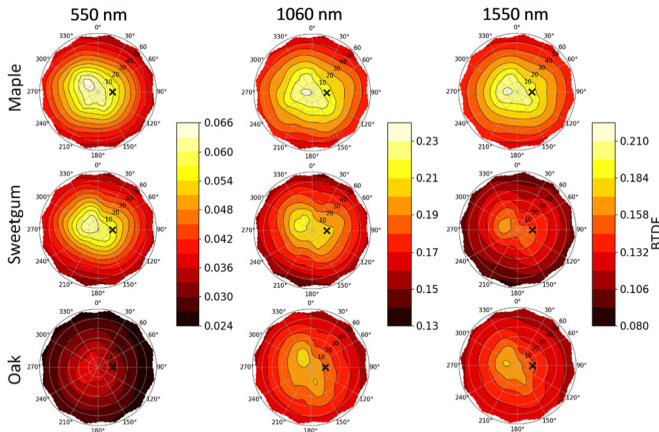

Fig. 8. Leaf BTDF at a 15° illumination angle. (From top to bottom) Rows are the maple, sweetgum, and oak leaf measurements. (From left to right) Wavelengths shown are 550, 1060, and 1550 nm. The illumination angle is marked by a black X while the axial rings are in 10° increments out to 60°. White space within the polar plot signifies either no data or omitted outlier data.

models, as explained in [7]. We selected the Smith GGX microfacet model as a starting point, as it had previously been evaluated for directional transmission [35]–[38]. Microfacet physically based models have become the standard within the graphics community, while the Smith GGX model has the advantage of improved accuracy, accounting for the projected

area of the microfacets [38]. The mathematical symbols and descriptions for the BTDF model development for this section are found in Table I.

The model created for this study consists of both a diffuse and specular component, as implemented by Bousquet *et al.* [9], but also includes an attenuation factor, T, which modulates the transmission of the specular component

$$\tau(\omega_o, \omega_i) = \tau_{\text{diff}}(\omega_o, \omega_i) + \tau_{\text{spec}}(\omega_o, \omega_i)T \qquad (5)$$

where $\tau(\omega_o, \omega_i)$ is the BTDF, ω_o is the view vector, and ω_i is the illumination vector. We assume illumination source azimuthal isotropy [11] and set the illumination azimuth vector to zero, making the incident vector (vector pointing toward the source)

$$\omega_i = \begin{bmatrix} \sin\theta_i \\ 0 \\ \cos\theta_i \end{bmatrix} \qquad (6)$$

where θ_i as the source zenith angle. The observation vector (vector pointing toward receiver) is then

$$\omega_o = \begin{bmatrix} \sin\theta_o \cos\phi_o \\ \sin\theta_o \sin\phi_o \\ \cos\theta_o \end{bmatrix} \qquad (7)$$

with ϕ_o being the azimuth observation angle and θ_o the zenith observation angle. The vectors were coded for θ_o and ϕ_o values over the hemisphere. This creates an array that is of the size

This article has been accepted for inclusion in a future issue of this journal. Content is final as presented, with the exception of pagination.

ROTH *et al.*: LEAF BTDF ESTIMATES AND MODELS FOR SELECT DECIDUOUS TREE SPECIES 7

Symbol	Description
$a(\omega_o)$	masking-shadowing associated function, weighted slope of the outgoing direction
α	roughness parameter
α_2	weight for relative contribution of each slab in dual-microfacet model $0 \leq \alpha_2 \leq 1$
β	optical depth
c	Fresnel associated function
$D(\omega_{h_t})$	microfacet distribution term
$\left\| \dfrac{\partial \bar{\omega}_{h_t}}{\partial \bar{\omega}_o} \right\|$	Jacobian term
$F(\omega_i, \omega_{h_t})$	Fresnel term
$G_2(\omega_i, \omega_o, \omega_{h_t})$	masking-shadowing term
g	Fresnel associated function
$\Lambda(\omega_i)$	masking-shadowing associated function, also known as Smith Lambda function
k_L	Lambertian coefficient
n_i	real part of index of refraction of air
n_t	real part of index of refraction of material
ω_i	illumination vector
ω_o	observation vector
ω_{h_t}	microfacet normal vector (top rough, bottom smooth slab)
ω_{h_b}	microfacet normal vector (top smooth, bottom rough slab)
ω_i'	internal incident vector (within the slab)
ω_{i_m}	internal incident angle weighted by index of refraction
ω_o'	internal observation vector (within the slab)
ω_{o_m}	internal observation vector weighted by index of refraction
ω_{z_+}	macro-surface normal vector, i.e. [0,0,1]
ϕ_o	azimuth observation angle
$T(\theta_{o\alpha}')$	specular attenuation term
$\tau(\omega_o, \omega_i)$	BTDF as a function of the illumination vector
$\tau_{diff}(\omega_o, \omega_i)$	diffuse component of the BTDF
$\tau_{spec}(\omega_o, \omega_i)$	specular component of the BTDF
$\tau_t(\omega_o, \omega_i)$	specular BTDF from rough top-side and smooth bottom-side slab
$\tau_b(\omega_o, \omega_i)$	specular BTDF from smooth top-side and rough bottom-side slab
θ_i	illumination source zenith angle
θ_m	microfacet normal vector
θ_o	zenith observation angle
$\theta_{o\alpha}'$	combination of the internal scattering angles of the two slabs used in the dual-microfacet model
θ_{o_b}'	internal scattering angles (top smooth, bottom rough slab)
θ_{o_t}'	internal scattering angle (top rough, bottom smooth slab)
X^+	step function, equaling one when greater than zero and zero otherwise

$[3, N_{\phi_o}, M_{\theta_o}]$, with N_{ϕ_o} being the number of ϕ_o samples and M_{θ_o} being the number of θ_o samples. The diffuse component of the BTDF is constant over all incident and observation vectors and is defined according to

$$\tau_{\text{diff}}(\omega_o, \omega_i) = \frac{k_L}{\pi} \quad (8)$$

where k_L is the Lambert coefficient. Note that the BTDF is also a function of wavelength, but this is not explicitly shown in the equations here for simplicity. The specular component fit used a modified dual-microfacet model proposed by Dai *et al.* [39], while also incorporating the GGX distribution of microfacets and Smith shadow-masking function, outlined in [36]–[38], for the microfacet surfaces.
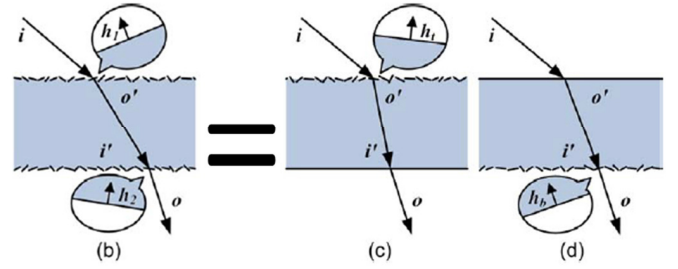

Fig. 9. Dual-microfacet model approximates an actual material slab (b) as a linear combination of two slabs. One slab (c) is top-side rough and bottom-side smooth, while the (d) second is top-side smooth and bottom-side rough (figure adapted from Dai *et al.* [39] with permission from publisher). Image (a) is not shown, but represents a dual sided smooth slab in [39].

The specular component is a modified dual-microsurface model, which models scattering by a pair of parallel micro-surfaces as a log-space mixture of the BTDFs of two basis slabs

$$\ln \tau_{\text{spec}}(\omega_o, \omega_i) = \alpha_2 \ln \tau_t(\omega_o, \omega_i) + (1 - \alpha_2) \ln \tau_b(\omega_o, \omega_i) \quad (9)$$

where $0 \leq \alpha_2 \leq 1$ weights the relative contribution of each slab. We use this slab-based approach to more realistically describe light scattering into a region of higher refractive index, i.e., the interior of the leaf, then back out into air. As shown in Fig. 9, the first slab consists of a rough top-side and smooth bottom-side, while the second is the opposite configuration, a smooth top-side and rough bottom-side. Note we use single scattering Fresnel facets for our model.

This decomposition allows for efficient computing, as the smooth surface results in only a Fresnel refraction and dampening, without diffusion. The model eliminates the computationally-expensive convolution needed if both top and bottom sides were rough. One of the major assumptions in the model is that the offset between the locations of the refraction at each of the two surfaces can be ignored. Another assumption is that the BTDF can be approximated as a combination of the two types of slabs mentioned. The combination of the two models occurs in log space, as the transmission effect is multiplicative. The model therefore is a kind of geometric interpolation, such that $\alpha_2 = (1/2)$ is a proper geometric mean. The dual microfacet model derivations are described in [39], while for completeness we provide here the required equations used in model computations. The top-side rough term obeys

$$\tau_t(\omega_o, \omega_i) = \left(\left\| \frac{\partial \bar{\omega}_{h_t}}{\partial \bar{\omega}_o} \right\| |\omega_i \cdot \omega_{h_t}| \left(1 - F(\omega_i, \omega_{h_t})\right) \right.$$
$$\left. \times \frac{\left(1 - F(\omega_i', \omega_{z^+})\right) G_2(\omega_i, \omega_o, \omega_{h_t}) D(\omega_{h_t})}{|\omega_i \cdot \omega_{z^+}| |\omega_o \cdot \omega_{z^+}|} \right). \quad (10)$$

The equation consists of Fresnel terms $F(\omega_i, \omega_{h_t})$ and $F(\omega_i', \omega_{z^+})$, the masking-shadowing $G_2(\omega_i, \omega_o, \omega_{h_t})$, the microfacet distribution $D(\omega_{h_t})$, and the Jacobian $\left\| (\partial \bar{\omega}_{h_t} / \partial \bar{\omega}_o) \right\|$ to relate the micro- to macro-surface. The terms in the denominator result from the fundamental constraint that the projected area of the geometric surface equals the projected

area of visible microsurfaces [38]. The Jacobian term equals

$$\left\| \frac{\partial \bar{\omega}_{h_t}}{\partial \bar{\omega}_o} \right\| = \frac{\left| \omega_o \cdot \omega_{o_m} \right| \left| \omega_{o_m} \cdot \omega_{h_t} \right|}{\left(\frac{n_t}{n_i} \right)^2 \left(\omega_i \cdot \omega_{h_t} + \omega_{o_m} \cdot \omega_{h_t} \right)^2}. \quad (11)$$

The microfacet normal vector ω_{h_t} is

$$\omega_{h_t} = -\frac{\omega_i + \omega_o - \left\| \omega_o - \omega_{o_m} \right\| \omega_{z_+}}{\left\| \omega_i + \omega_{o_m} \right\|}. \quad (12)$$

The internal observation vector, ω_o', derives from Snell's law, which for the 3-D model geometry, assuming the z-axis is perpendicular to the slab surface, has the form

$$\omega_o' = \frac{n_i}{n_t} \begin{bmatrix} \omega_{o_x} \\ \omega_{o_y} \\ -\sqrt{\left(\frac{n_t}{n_i} \right)^2 - \omega_{o_x}^2 - \omega_{o_y}^2} \end{bmatrix} \quad (13)$$

where ω_{o_m} obeys

$$\omega_{o_m} = \frac{n_t}{n_i} \omega_o' \quad (14)$$

and where n_t and n_i are the index of refraction of the material and air, respectively. The internal incident vector onto the second plate is merely the negative of the outgoing vector from the first plate

$$\omega_i' = -\omega_o' \quad (15)$$

and the surface normal for the second plate is just the macro surface normal vector

$$\omega_{z_+} = \begin{bmatrix} 0 \\ 0 \\ 1 \end{bmatrix}. \quad (16)$$

We used the shadow masking function for transmission, defined by Heitz *et al.* [37]

$$G_2 = \mathrm{B}(1 + \Lambda(\omega_i), 1 + \Lambda(\omega_o)) \quad (17)$$

with B being the Beta function and Λ defined as

$$\Lambda(\omega_o) = \frac{-1 + \sqrt{1 + \frac{1}{a(\omega_o)^2}}}{2} \quad (18)$$

and

$$a(\omega_o) = \frac{1}{\alpha \tan \theta_o} \quad (19)$$

where α, the roughness, is a fundamental model fitting parameter.

Unlike in [39], who found their distribution function through regression, we used the GGX distribution, $D(\omega_{h_t})$, which obeys

$$D(\omega_{h_t}) = \frac{\mathrm{X}^+ (\omega_{h_t} \cdot \omega_{z_+})}{\pi \alpha^2 \cos^4 \theta_m \left(1 + \frac{\tan^2 \theta_m}{\alpha^2} \right)^2}. \quad (20)$$

X^+ is the step function equaling one when $\omega_{h_t} \cdot \omega_{z_+}$ is greater than one and zero when $\omega_{h_t} \cdot \omega_{z_+}$ is less than or equal to zero.

Note that $\omega_{h_t} \cdot \omega_{z_+} = \cos\theta_m$, which is the z component of the ω_{h_t} unit vector. The Fresnel factor, as shown in [36], obeys

$$F(\omega_i, \omega_m) = \frac{1}{2} \frac{(g - c)^2}{(g + c)^2} \left(1 + \frac{(c(g + c) - 1)^2}{(c(\mathrm{g-c}) + 1)^2} \right) \quad (21)$$

$$g = \sqrt{\frac{n_t^2}{n_i^2} - 1 + c^2} \quad (22)$$

$$c = \left| \omega_i \cdot \omega_{z_+} \right|. \quad (23)$$

Note that for air, $n_i \approx 1$. For the second surface Fresnel calculation, caution must be taken to switch the indices of refraction, because now the light is moving from a region with a larger index of refraction to a lower index of refraction. Thus, for the second interface $g = \sqrt{(n_i^2/n_t^2) - 1 + c^2}$ and $c = \left| \omega_i' \cdot \omega_{z_+} \right|$.

The top-side smooth, bottom-side rough slab BTDF, $\tau_b(\omega_o, \omega_i)$, formula similarly obeys

$$\tau_b(\omega_o, \omega_i) = \left(\left\| \frac{\partial \bar{\omega}_{h_b}}{\partial \bar{\omega}_o} \right\| \left| \omega_i' \cdot \omega_{h_b} \right| \left(1 - F\left(\omega_i', \omega_{h_b} \right) \right) \right.$$
$$\left. \times \frac{\left(1 - F\left(\omega_i', \omega_{z^+} \right) \right) G\left(\omega_i, \omega_o, \omega_{h_b} \right) D\left(\omega_{h_b} \right)}{\left| \omega_i' \cdot \omega_{z^+} \right| \left| \omega_o \cdot \omega_{z^+} \right|} \right) \quad (24)$$

with the major difference this time being that all functions are now for a smooth top-side and a rough bottom-side. The Jacobian term now is

$$\left\| \frac{\partial \bar{\omega}_{h_b}}{\partial \bar{\omega}_o} \right\| = \frac{\left| \omega_o \cdot \omega_{h_b} \right|}{\left(\omega_{i_m} \cdot \omega_{h_b} + \omega_o \cdot \omega_{h_b} \right)^2}. \quad (25)$$

The bottom-side microfacet normal now becomes

$$\omega_{h_b} = -\frac{\omega_i + \omega_o + \left\| \omega_i - \omega_{i_m} \right\| \omega_{z_+}}{\left\| \omega_o + \omega_{i_m} \right\|} \quad (26)$$

with

$$\omega_i' = \frac{n_i}{n_t} \begin{bmatrix} \omega_{i_x} \\ \omega_{i_y} \\ \sqrt{\left(\frac{n_t}{n_i} \right)^2 - \omega_{i_x}^2 - \omega_{i_y}^2} \end{bmatrix} \quad (27)$$

$$\omega_{i_m} = \frac{n_t}{n_i} \omega_i'. \quad (28)$$

The Fresnel terms, masking-shadowing term, and microsurface distribution function are all the same as previously defined for the top-rough and bottom-smooth BTDF. The specular attenuation model term used Beer's law [40], incorporating an optical depth term, β, and normalized length $(1/\cos(\theta_{oa}'))$

$$T(\theta_{oa}') = e^{-\frac{\beta}{\cos(\theta_{oa}')}}. \quad (29)$$

This approach applied Beer's law to the BTDF model internal scattering vector. θ_{oa}' is a combination of the internal scattering angles of the two slabs used in the model

$$\theta_{oa}' = \alpha_2 \theta_{o_t}' + (1 - \alpha_2) \theta_{ob}'. \quad (30)$$

The α_2 term is the same as previously defined in (9) and determines the weight between the two BTDF calculations of $\tau_t(\omega_o, \omega_i)$ and $\tau_b(\omega_o, \omega_i)$. There will be a different θ_{oa}'
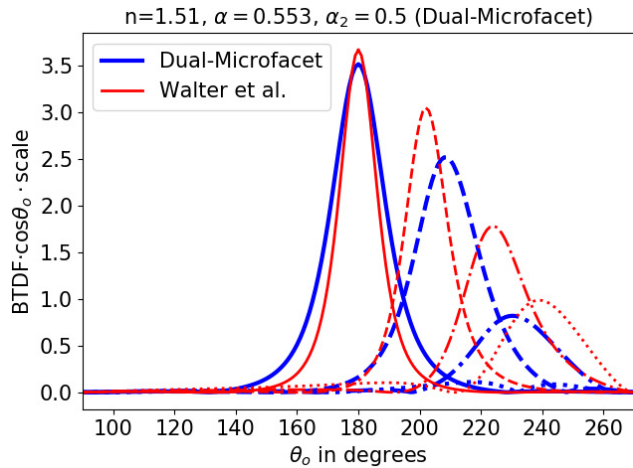
Fig. 10. Comparison of the principle plane BTDF between our modified dual microfacet model, blue plot lines, and that from reproducing plots from Walter *et al.* [36] representing the Smith GGX single-scattering model, red plot lines. Both are plotted for incident angles at 0°, 30°, 60°, and 80° marked by solid, dashed, dashed-dot, and dotted lines, respectively.

for every observation zenith angle θ_o, and azimuth angle ϕ_o. This creates an array of transmissions, equivalent in size to $\tau_{\text{spec}}(\omega_o, \omega_i)$. The fundamental parameters that characterize the BTDF then are the roughness parameter α, index of refraction n_t, the Lambert coefficient k_L, the weight factor α_2, and the optical density β.

We compared our results to the principle plane plots found in [36] in order to confirm the accuracy of our version of the dual microfacet model (specular component). One of the comparisons is seen in Fig. 10. The plots from Walter *et al.* [36] described a single scattering surface into a region of higher index of refraction, so we do not expect the plots to be the same, but they should exhibit similarities. We plot $\tau_{\text{spec}}(\omega_o, \omega_i) \cos(\theta_o)$ along with scaling factors needed to match Walter *et al.*'s [36] published, but uncalibrated measurements. For single scattering, Walter *et al.* [36] also multiplied his results by a radiance-scaling factor of $(n_i/n_o)^2$ to account for conservation of energy when scattering into a higher index of refraction. The dual microfacet model does not require radiance scaling, since light propagation in this model begins and ends in a region with the same index of refraction.

As expected, the higher illumination incident zenith angles produce less transmission in the dual microfacet model than in the single scattering layer. This is primarily due to the presence of a second interface causing more reflection, as well as reduced transmission. Also, notice that the locations of the specular peaks in the dual microfacet model are closer to 180° from the incident direction, thus producing less deviation of emerging rays. This is to be expected, as light rays coming out of a slab of higher index of refraction will refract back toward the original incident direction of the first interface. Stated differently, the light ray would perfectly refract back to its original direction, if both sides of the slab were perfectly smooth.

V. MODELING RESULTS

Our model fits used the Levenberg–Marquardt nonlinear least squares minimization from the python package

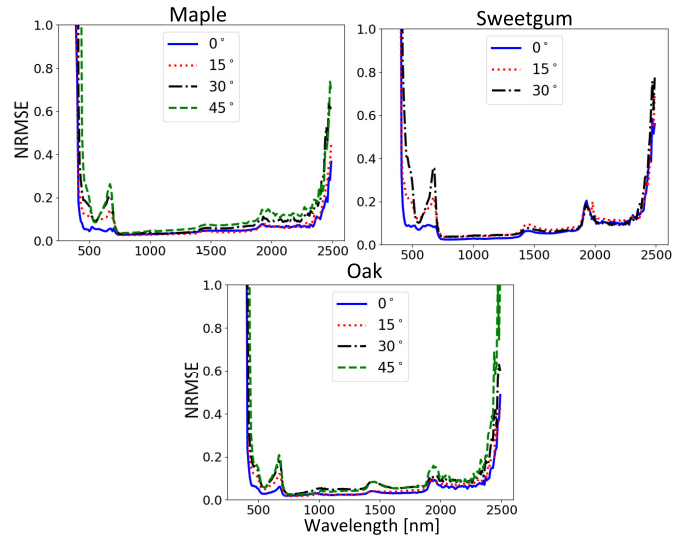|	k_l	n_t	α	α_2	β
Initial value	.3	1.5	1	.4	1
Lower bound	.003	1	.2	.2	.001
Upper bound	.6	2.5	3	.8	4

Fig. 11. NRMSE to the model found from least-squares minimization for each of the three leaf types, namely, maple, sweetgum, and oak, over the spectrum (350–2500 nm). The plots are for the four illumination angles: 0°, 15°, 30°, and 45°, except for the sweetgum leaf which was only fit for the three illumination angles: 0°, 15°, and 30°.

LMFIT [41]. The first step consists of concatenating all directional measurements for each illumination and leaf type. Similarly, we concatenated the model values at the equivalent observation angles for the same illumination angles. We then used least squares minimization according to the following equation:

$$X^2 = \sum_{\theta_i, \theta_o, \phi_o} (\tau(\omega_o, \omega_i)_{\text{measured}} - \tau(\omega_o, \omega_i)_{\text{modeled}})^2. \quad (31)$$

Minimization was accomplished for each captured wavelength in 1-nm steps. Both physical constraints and experimentation allowed us to establish initial values and bounds for the parameters to be optimized. The initial values and bounds are given in Table II.

As a metric, we define a normalized root-mean-squared error by dividing the root-mean-squared error by the mean. We then computed the normalized root-mean-squared error (NRMSE) for each measurement cycle at each wavelength as seen in Fig. 11. We also computed the mean NRMSE for each leaf type over a narrower wavelength range from 450 to 2300 nm, (in order to exclude high noise wavelength regions), with results given in Table III. A mean of these values gives a total NRMSE of 6.8%.

The NRMSE values in Fig. 11 appear to be high, specifically in a few wavelength bands. This can be explained by the fact that the model fit encompasses each of the different leaves at all illumination angles. Another reason is that the model

TABLE III

MEAN NRMSE VALUES FOR THE 450–2300-nm WAVELENGTH RANGE FOR THE THREE LEAF TYPES

	NRMSE
Maple	.065
Sweetgum	.081
Oak	.057
Total Mean	**.068**

can only place a symmetrical non-Lambertian component on the principle axis, while actual measurements may show the non-Lambertian component slightly off axis due to natural leaf asymmetries. This scenario is most pronounced where the Lambertian component is minimized in the absorption bands. Extremely high NRMSE values are seen below 450 nm and above 2300 nm where the low detector responsivity causes significant noise [42]. Also, the leaf transmittance drops significantly below 450 nm, resulting in lower SNR and larger relative error.

The fit parameters seen in Fig. 12 are especially noisy toward longer wavelengths. This is largely due to the higher noise level of the data in this part of the spectrum. We used a "multi-regression stability" function analysis, which seeks input parameters that result in consistent results across wavelengths, in order to reduce some of the noise in regression. The parameter values are not expected to vary quickly across wavelengths, and we exploited this assumption to obtain more stable solutions. The algorithm evaluates the previous regression values and compares them to the current results, as the program iterates over wavelengths. We chose the index of refraction as the stability threshold variable, since, while variable, it still exhibited high correlation. For example, if the difference between the previous wavelength fit parameter and current fit parameter was greater than some threshold, we changed the starting regression values for each parameter to a value halfway between the previous and current values. We set the maximum multi-regression iteration count to three. Three iterations yielded good results, balancing convergence and computation time. This resulted in smoother spectral outputs, while avoiding observed local minima around the global minimum.

The pattern seen over wavelength in the optimized parameters in Fig. 12 is very similar for each of the three leaf types. Note, that the sweetgum leaf was only fit to data from three source zenith angles: 0°, 15°, and 30°, while the maple and oak leaves were fit to all four source angles. The sweetgum parameters exhibited some stark contrasts to the other two leaf types when fit to all four source angles. As mentioned earlier, the sweetgum measurement with the 45° illumination angle did not follow the pattern of becoming more diffuse with larger illumination zenith angle, which we attributed to between-leaf variation. Fitting the model with the 0°, 15°, and 30° illumination angles, as seen in Fig. 11, resulted in model NRMSE for the sweetgum leaf dropping slightly, but more significant is the fact that the parameter values followed the same trend spectrally, as seen for the maple and oak leaves. We therefore only show the sweetgum fit here to
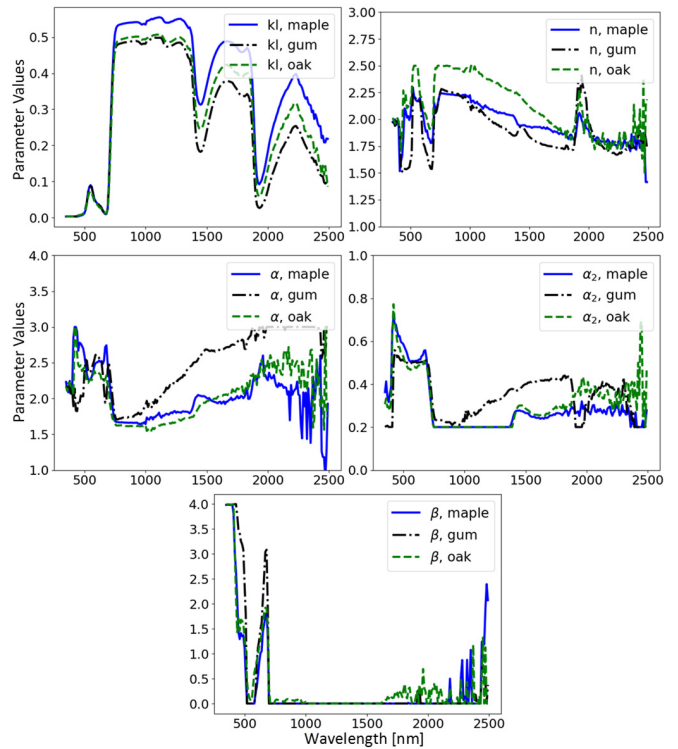
Fig. 12. (From left to right, top to bottom) Fit parameters for each leaf type over the spectrum (350–2500 nm): the diffuse component, kl; index of refraction, n; roughness, α; ratio of top versus bottom dual microfacet model, α_2; and optical density, β. The sweetgum parameters are from the optimization using only 0°, 15°, and 30° illumination angles, while oak and maple are from the fit to all four illumination angles.
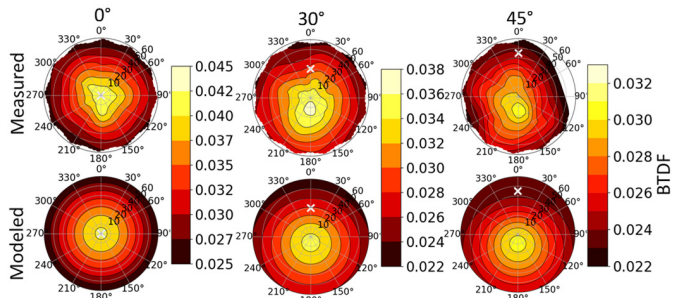

Fig. 13. Comparison of (Top row) measured BTDF values and (Bottom row) modeled BTDF values for the oak leaf. (From left to right) Comparison is for zenith illumination angles of 0°, 30°, and 45°. The white X denotes the illumination angle position.

the three illumination angles: 0°, 15°, and 30°, while all the measurements and fits are available in the published data for completeness.

As expected, the diffuse component seen in Fig. 12 is patterned after a typical vegetation spectrum. Leaf thickness and surface properties likely dictated the diffuse magnitudes, with the maple leaf being the thinnest and clearly exhibiting the strongest values. However, the sweetgum leaf clearly has the smallest diffuse component, which is most notable in the SWIR, possibly due to differences in leaf chemical content and leaf anatomy. The index of refraction overall is similar in scale for the three leaves, correlating slightly with absorption spectra in the chlorophyll absorption regions, increasing in
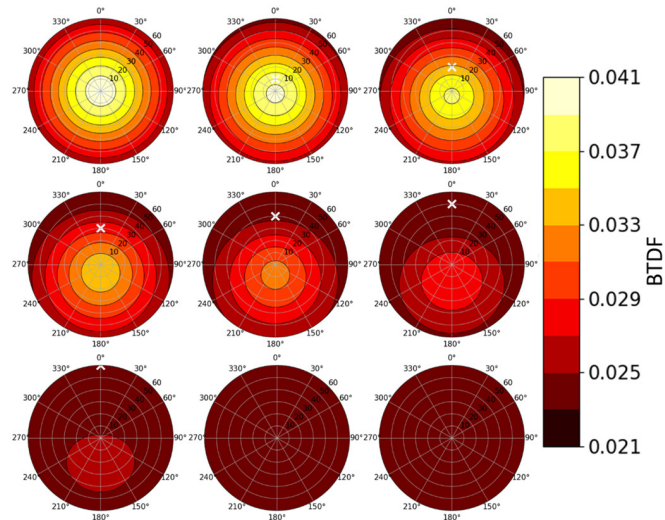
Fig. 14. BTDF model for the oak leaf at 550 nm in 10° steps from (Top left) 0° to (Bottom right) 80°. The model results in an expected BTDF pattern, showing the strongest specular component at nadir illumination, and becoming more diffuse with increasing illumination zenith angle.

TABLE IV
CORRELATION COEFFICIENTS FOR HIGHEST CORRELATED VARIABLES
FOR THE OAK LEAF

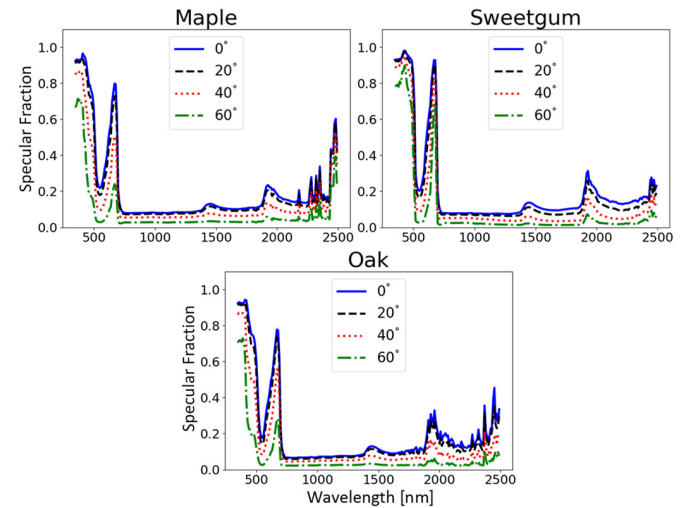|	k_l, n	n, β	α, β	k_l, α	k_l, β	n, α
450 nm	-0.66	-0.75	-0.60	0.53	0.23	-
550 nm	-0.79	-0.77	-0.47	0.52	0.41	-.19
650 nm	-0.64	-0.50	-0.78	0.44	-	-.13
850 nm	-0.89	-0.65	-0.42	0.472	0.51	-.41
1060 nm	-0.84	-0.612	-0.477	0.452	0.468	-0.392
1550 nm	-0.75	-0.48	-0.67	0.39	0.30	-0.31
2050 nm	-0.642	-0.473	-0.770	0.380	0.146	-0.182
Mean	-0.74	-0.60	-0.60	0.45	0.34	-0.27

Fig. 15. (From left to right, top to bottom) Specular fraction plots over the spectrum (350–2500 nm) of maple, sweetgum, and oak leaves. The plots include the specular fraction at illumination angles of 0°, 20°, 40°, and 60°. Note that as the illumination zenith angles increase, the specular fraction decreases.

the near infrared response (NIR), with a gradual drop in the SWIR, but exhibiting a spike in the 1800–2000-nm water absorption spectral regions. Values for the refractive index are greater than expected [9]. The linear combination used for the specular component and the high correlation between variables in the model are possible causes for the higher than anticipated values. The roughness parameter, α, is higher in the visible, decreases before the NIR, and increases toward the NIR and SWIR domains. The sweetgum leaf has the strongest increase in the NIR and SWIR overall, having the largest value of the three leaves. The α_2 parameter exhibits a similar trend for each leaf, being slightly higher in the visible, and lower in the NIR and SWIR spectral regions. A larger α_2 implies that the top-side rough bottom-side smooth was given more weight. Top-side rough (i.e., a larger α_2) according to the model exhibits less diffraction. The β parameters for each leaf exhibit an optical density spike between 550 and 700 nm, with the sweetgum having the largest peak, suggesting that it has the highest absorption. It is challenging to link the five parameters in the model to actual leaf physiology, although select relationships may exist, the variables are highly correlated. We therefore can say that the roughness and index of refraction parameters are related to, but not absolute measurements of the actual leaf physical characteristics. Future work should study the link between microfacet models and actual leaf physiology.

Table IV gives the highest correlations for the oak leaf and their correlation coefficients at a few selected wavelengths, as computed by LMFIT. Each leaf fit exhibited similar correlations. The diffuse term and the index of refraction show the largest correlation, which is due to the behavior of the index of refraction: when increased, the specular peak moves toward nadir, broadens, and decreases, thus resembling the bias diffuse term. β is the attenuation term, and its correlation with the index of refraction arises from the reduction in the specular peak when the index of refraction increases. When α increases, the specular peak moves toward nadir and

decreases, but without significantly changing shape. The α and β correlation stems from the fact that both parameters influence the magnitude of the specular peak.

A visual, qualitative assessment shows a good fit between polar plots of measurements and the model BTDF. An example of the oak leaf measurements and model fits at 550 nm appears in Fig. 13. Fig. 14 displays the extension of the model to nonmeasured illumination zenith angles, which follows expectations of becoming more diffuse at larger angles.

Our modeled results included a specular fraction analysis, which first computes DHT_{spec} according to (4) for only the specular modeled component, $\tau_{\text{spec}}(\omega_o, \omega_i)$ and then calculates a specular fraction (fractional contribution of specular transmittance to total DHT) via

$$\text{Specular Fraction} = \frac{\text{DHT}_{\text{spec}}}{\text{DHT}_{\text{spec}} + k_l} \tag{32}$$

where k_l is the diffuse term of the model. In Fig. 15, we plot the specular fraction for the three leaf species and four illumination angles.

Correlations exist between model parameters, making the specular fraction presented relative. Although a relative value, it is still valuable in identifying wavelengths where

non-Lambertian scattering dominates. The plots show a strong peak in one of the chlorophyll absorption bands (600–700 nm), where the specular component dominates with minimal diffuse component. There are also smaller peaks in the water absorption bands between 1400–1500 and 1900–2000 nm. The sweetgum leaf has the strongest specular fraction components overall, with the oak and maple being very similar. This was attributed to the sweetgum leaf's characteristics of being thin and glossy, causing the least diffuse transmission scattering, when compared with the rougher maple leaf, and the thicker oak leaf.

VI. CONCLUSION

This study described the leaf directional transmittance scattering measurements and modeling for Norway maple (*Acer platanoides*), American sweetgum (*Liquidambar styraciflua*), and northern red oak (*Quercus rubra*), collected via the GRIT-T goniometer [24]–[28]. In general, the sweetgum and maple leaf exhibited strong directional transmission components, the maple presented the greatest transmittance, and the oak leaf transmittance was the most diffuse. These results can be attributed to the leaf appearances of the sweetgum being thin and glossy, the maple very thin and matte, and the oak having the thickest cuticle layer. We developed a two-layered microfacet model, following the technique presented by Dai *et al.* [39], while incorporating the Smith masking-shadowing function [35], the GGX microfacet distribution [38], and an optical density with Beer's law [40]. Nonlinear least squares minimization of the model to the measurements resulted in an overall 6.8% mean NRMSE averaged over the wavelengths 450–2300 nm. The model fit parameters represent the physical leaf characteristics of the index of refraction, roughness, top versus bottom boundary roughness ratio, optical density, and a Lambertian term. The model enables the capability to produce BTDF values for all possible illumination and view directions necessary for the integration into radiative transfer simulations. High correlations between the model parameters, and physically unrealistic values, made it difficult to directly relate the parameters to leaf structure. The model depended on the summation of separately modeled diffuse and specular components of the leaf BTDF. We analyzed the specular fraction, defined as the ratio between the non-Lambertian component of the BTDF and the total transmission. For a nadir illumination angle in the chlorophyll absorption region at 670 nm, the directional component is strongest, being 80% or more of the total transmittance. The sweetgum leaf showed the strongest specular fraction component, while the oak and maple were very similar. Future work should focus on determining the contribution of the leaf directional transmittance component to the signal observed by canopy-level remote-sensing systems. We also believe leaf BTDF will have significant impact on remote-sensing modalities such as PAR measurements looking up into the canopy. Future efforts also could assess the connection between the model inputs and leaf physiology. Another important advancement in leaf-level measurements would be to create larger data sets for the same leaf type and measurement method to use in a statistical analysis in order to more accurately determine error due to leaf variability. In conclusion, this study contributes to the scientific advancement of spectral measurements based on the following: 1) novel high spectral resolution broad leaf BCTF measurements, while having 2) identified distinguishing features between three leaf species; 3) developed a highly accurate leaf BTDF model, which incorporates methods from the computer graphics community; 4) extracted model parameters related to leaf physiology; and 5) identified wavelengths in which single scattering predominates over Lambertian transmission. This work provides insights into light vegetation interactions at the leaf-level, enables future advances in remote-sensing radiative transfer simulations and allows for further development of canopy-level BSDF models.

REFERENCES

[1] F. E. Nicodemus, J. C. Richmond, J. J. Hsia, I. W. Ginsberg, and T. Limperis, "Geometrical Considerations and Nomenclature for Reflectance," NBS Mono., Washington, DC, USA, Tech. Rep., 1977.

[2] G. Schaepman-Strub, M. E. Schaepman, T. H. Painter, S. Dangel, and J. V. Martonchik, "Reflectance quantities in optical remote sensing— Definitions and case studies," *Remote Sens. Environ.*, vol. 103, no. 1, pp. 27–42, 2006, doi: 10.1016/j.rse.2006.03.002.

[3] J. V. Martonchik, C. J. Bruegge, and A. H. Strahler, "A review of reflectance nomenclature used in remote sensing," *Remote Sens. Rev.*, vol. 19, nos. 1–4, pp. 9–20, Dec. 2000.

[4] F. O. Bartell, E. L. Dereniak, and W. L. Wolfe, "The theory and measurement of bidirectional reflectance distribution function (BRDF) and bidirectional transmittance distribution function (BTDF)," *Proc. SPIE*, vol. 0257, Mar. 1981, Art. no. 959611.

[5] F. B. Leloup, S. Forment, P. Dutré, M. R. Pointer, and P. Hanselaer, "Design of an instrument for measuring the spectral bidirectional scatter distribution function," *Appl. Opt.*, vol. 47, no. 29, pp. 5454–5467, 2008.

[6] B. Roth, "Broad leaf bidirectional scattering distribution functions (BSDFs)," *IEEE Data Port*, 2020, doi: 10.21227/yjek-2059.

[7] B. D. Roth, M. G. Saunders, C. M. Bachmann, and J. A. van Aardt, "On leaf BRDF estimates and their fit to microfacet models," *IEEE J. Sel. Topics Appl. Earth Observ. Remote Sens.*, vol. 13, pp. 1761–1771, 2020, doi: 10.1109/JSTARS.2020.2988428.

[8] (2019). *OPTICLEAF the Data Base on Leaf Optical Properties*. [Online]. Available: http://opticleaf.ipgp.fr/index.php?page=database

[9] L. Bousquet, S. Lachérade, S. Jacquemoud, and I. Moya, "Leaf BRDF measurements and model for specular and diffuse components differentiation," *Remote Sens. Environ.*, vol. 98, nos. 2–3, pp. 201–211, Oct. 2005, doi: 10.1016/j.rse.2005.07.005.

[10] R. L. Cook and K. E. Torrance, "A reflectance model for computer graphics," *ACM Trans. Graph.*, vol. 1, no. 1, pp. 7–24, Jan. 1982, doi: 10.1145/357290.357293.

[11] D. Biliouris *et al.*, "RPV model parameters based on hyperspectral bidirectional reflectance measurementsof Fagus sylvatica L. Leaves," *Remote Sens.*, vol. 1, no. 2, pp. 92–106, 2009, doi: 10.3390/rs1020092.

[12] H. Rahman, B. Pinty, and M. M. Verstraete, "Coupled surface-atmosphere reflectance (CSAR) model: 2. Semiempirical surface model usable with NOAA advanced very high resolution radiometer data," *J. Geophys. Res., Atmos.*, vol. 98, no. D11, pp. 20791–20801, 1993, doi: 10.1029/93JD02072.

[13] D. Xie, W. Qin, P. Wang, Y. Shuai, Y. Zhou, and Q. Zhu, "Influences of leaf-specular reflection on canopy BRF characteristics: A case study of real maize canopies with a 3-D scene BRDF model," *IEEE Trans. Geosci. Remote Sens.*, vol. 55, no. 2, pp. 619–631, Feb. 2017, doi: 10.1109/TGRS.2016.2598442.

[14] B. Yang, Y. Knyazikhin, H. Zhao, and Y. Ma, "Contribution of leaf specular reflection to canopy reflectance under black soil case using stochastic radiative transfer model," *Agricult. Forest Meteorol.*, vol. 263, pp. 477–482, Dec. 2018, doi: 10.1016/j.agrformet.2018.08.024.

[15] D. Combes, L. Bousquet, S. Jacquemoud, H. Sinoquet, C. Varlet-Grancher, and I. Moya, "A new spectrogoniophotometer to measure leaf spectral and directional optical properties," *Remote Sens. Environ.*, vol. 109, no. 1, pp. 107–117, Jul. 2007, doi: 10.1016/j.rse.2006.12.007.

[16] E. A. Walter-Shea, "Laboratory and field measurements of leaf spectral properties and canopy architecture and their effects on canopy reflectance," M.S. thesis, Univ. Nebraska, Lincoln, NE, USA, 1987.

[17] T. W. Brakke, J. A. Smith, and J. M. Harnden, "Bidirectional scattering of light from tree leaves," *Remote Sens. Environ.*, vol. 29, no. 2, pp. 175–183, 1989, doi: 10.1016/0034-4257(89)90025-4.

[18] T. W. Brakke, "Specular and diffuse components of radiation scattered by leaves," *Agricult. Forest Meteorol.*, vol. 71, nos. 3–4, pp. 283–295, 1994, doi: 10.1016/0168-1923(94)90016-7.

[19] M. A. Greiner, B. D. Duncan, and M. P. Dierking, "Bidirectional scattering distribution functions of maple and cottonwood leaves," *Appl. Opt.*, vol. 46, no. 25, p. 6485, Sep. 2007, doi: 10.1364/ao.46.006485.

[20] S. Jacquemoud and L. S. Ustin, "Modeling leaf optical properties," *Photobiol. Sci. Online*, 2008. [Online]. Available: http://photobiology.info/Jacq_Ustin.html

[21] B. D. Roth, A. A. Goodenough, S. D. Brown, J. A. van Aardt, M. G. Saunders, and K. Krause, "Simulations of leaf BSDF effects on lidar waveforms," *Remote Sens.*, vol. 12, no. 18, p. 2909, Sep. 2020.

[22] K. J. Stadt and V. J. Lieffers, "Comparing PAR transmission models for forest understorey vegetation," *Appl. Vegetation Sci.*, vol. 8, no. 1, pp. 65–76, May 2005, doi: 10.1111/j.1654-109X.2005.tb00630.x.

[23] J. D. Harms *et al.*, "Fully automated laboratory and field-portable goniometer used for performing accurate and precise multiangular reflectance measurements," *J. Appl. Remote Sens.*, vol. 11, no. 4, 2017, Art. no. 046014, doi: 10.1117/1.jrs.11.046014.

[24] C. M. Bachmann, R. S. Eon, B. Ambeau, J. Harms, G. Badura, and C. Griffo, "Modeling and intercomparison of field and laboratory hyperspectral goniometer measurements with G-LiHT imagery of the Algodones Dunes," *J. Appl. Remote Sens.*, vol. 12, no. 1, 2017, Art. no. 012005, doi: 10.1117/1.JRS.12.012005.

[25] R. Eon, C. Bachmann, and A. Gerace, "Retrieval of sediment fill factor by inversion of a modified hapke model applied to sampled HCRF from airborne and satellite imagery," *Remote Sens.*, vol. 10, no. 11, p. 1758, Nov. 2018, doi: 10.3390/rs10111758.

[26] G. P. Badura, C. M. Bachmann, A. C. Tyler, S. Goldsmith, R. S. Eon, and C. S. Lapszynski, "A novel approach for deriving LAI of salt marsh vegetation using structure from motion and multiangular spectra," *IEEE J. Sel. Topics Appl. Earth Observ. Remote Sens.*, vol. 12, no. 2, pp. 599–613, Feb. 2019, doi: 10.1109/JSTARS.2018.2889476.

[27] G. Badura, C. M. Bachmann, J. Harms, and A. Abelev, "Observed relationship between BRF spectral-continuum variance and macroscopic roughness of clay sediments," *IEEE Trans. Geosci. Remote Sens.*, vol. 57, no. 9, pp. 6726–6740, Sep. 2019, doi: 10.1109/TGRS.2019.2908170.

[28] G. Badura and C. M. Bachmann, "Assessing effects of azimuthally oriented roughness on directional reflectance of sand," *IEEE J. Sel. Topics Appl. Earth Observ. Remote Sens.*, vol. 12, no. 3, pp. 1012–1025, Mar. 2019, doi: 10.1109/JSTARS.2019.2896592.

[29] Edmund Optics. *Broadban Hybrid Diffusers Specification*. Accessed: Nov. 7, 2019. [Online]. Available: https://edmundoptics.com

[30] *Technical Guide: Integrating Sphere Theory and Applications*, Labsphere, North Sutton, NH, USA, 2017.

[31] P. J. Rousseeuw and C. Croux, "Alternatives to the median absolute deviation," *J. Amer. Stat. Assoc.*, vol. 88, no. 424, pp. 1273–1283, Dec. 1993.

[32] A. Hovi, P. Forsström, M. Mõttus, and M. Rautiainen, "Evaluation of accuracy and practical applicability of methods for measuring leaf reflectance and transmittance spectra," *Remote Sens.*, vol. 10, no. 2, p. 25, Dec. 2017, doi: 10.3390/rs10010025.

[33] R. B. Myneni and J. Ross, *Photon-Vegetation Interactions: Applications in Optical Remote Sensing and Plant Ecology*. Berlin, Germany: Springer, 2012.

[34] P. S. Nobel, "Photosynthetic rates of sun versus shade leaves of Hyptis emoryi Torr," *Plant Physiol.*, vol. 58, no. 2, pp. 218–223, Aug. 1976, doi: 10.1104/pp.58.2.218.

[35] B. G. Smith, "Geometrical shadowing of a random rough surface," *IEEE Trans. Antennas Propag.*, vol. 15, no. 5, pp. 668–671, Sep. 1967, doi: 10.1109/TAP.1967.1138991.

[36] B. Walter, S. R. Marschner, H. Li, and K. E. Torrance, "Microfacet models for refraction through rough surfaces," in *Proc. Eurograph. Symp. Rendering Techn.*, 2007, pp. 195–206.

[37] E. Heitz, J. Hanika, E. d'Eon, and C. Dachsbacher, "Multiple-scattering microfacet BSDFs with the smith model," *ACM Trans. Graph.*, vol. 35, no. 4, pp. 1–14, Jul. 2016, doi: 10.1145/2897824.2925943.

[38] E. Heitz, "Understanding the masking-shadowing function in microfacet-based BRDFs," *J. Comput. Graph. Techn.*, vol. 3, no. 2, pp. 48–106, 2014.

[39] Q. Dai, J. Wang, Y. Liu, J. Snyder, E. Wu, and B. Guo, "The dual-microfacet model for capturing thin transparent slabs," *Comput. Graph. Forum*, vol. 28, no. 7, pp. 1917–1925, Oct. 2009, doi: 10.1111/j.1467-8659.2009.01570.x.

[40] A. Beer, "Determination of the absorption of red light in colored liquids," *Ann. Phys. Chem.*, vol. 86, pp. 78–88, May 1852.

[41] M. Newville, T. Stensitzki, D. B. Allen, and A. Ingargiola, "Non-linear least-squares minimization and curve-fitting for Python," Tech. Rep., 2014, doi: 10.5281/zendo.598352.

[42] *Sectroradiometer Certificate of Calibration*, ASD, Boulder, CO, USA, 2017.

Benjamin D. Roth (Member, IEEE) received the B.S. degree in physics from the United States Air Force Academy, Colorado Springs, CO, USA, in 2007, and the M.S. degree in applied physics from the United States Air Force Institute of Technology, Wright-Patterson AFB, OH, USA, in 2012. He is pursuing the Ph.D. degree with the Chester F. Carlson Center for Imaging Science, Rochester Institute of Technology, Rochester, NY, USA.

His research is on improving light detection and ranging (lidar) data algorithms for forest ecological studies. His emphasis is on characterizing optical properties of deciduous tree leaves for use in lidar radiative transfer models.

M. Grady Saunders received the bachelor's degree (Hons.) from East Tennessee State University, Johnson City, TN, USA, in 2017, where he majored in digital media and minored in mathematics, and the master's degree in imaging science from the Rochester Institute of Technology, Rochester, NY, USA.

His scientific interests revolve around stocastic light transport simulation and procedural modeling techniques in the context of 3-D computer graphics and computer-generated environments.

Charles M. Bachmann (Senior Member, IEEE) received the A.B. degree in physics from Princeton University, Princeton, NJ, USA, in 1984, and the Sc.M. and Ph.D. degrees in physics from Brown University, Providence, RI, USA, in 1986 and 1990, respectively.

He was a Research Physicist with the Naval Research Laboratory, Washington, D.C., USA, from 1990 to 2013, where he served as the Head of the Coastal Science and Interpretation Section, Remote Sensing Division, from 2003 to 2013. From 2012 to 2013, through the U.S. Navy Engineer and Scientist Exchange Program, he was with the Defense Science Technology Organisation (DSTO) Maritime Division, Sydney, NSW, Australia. In 2013, he joined the Chester F. Carlson Center for Imaging Science (CIS), Rochester Institute of Technology (RIT), Rochester, NY, USA, as the Frederick and Anna B. Wiedman Chair. Since 2016, he has also been serving as the CIS Graduate Program Coordinator. He holds two U.S. patents for methods of analysis related to hyperspectral remote sensing imagery. His research focuses on hyperspectral remote sensing of coastal and desert environments, bidirectional reflectance factor (BRF), and radiative transfer modeling for retrieval of geophysical and biophysical parameters, field calibration and validation, the development of advanced instrumentation (goniometers), and abstract models for interpreting hyperspectral and multisensor imagery based on manifold descriptions and graph theory.

Jan van Aardt (Member, IEEE) received the Hons. Forestry degree in remote sensing and geographical information systems (GIS) and the B.Sc. Forestry degree (biometry and silviculture specialization) from the University of Stellenbosch, Stellenbosch, South Africa, and the M.S. and Ph.D. Forestry degrees from Virginia Polytechnic Institute and State University, Blacksburg, VA, USA, in 1998, 2000, and 2004, respectively.

He is a Professor with the Chester F. Carlson Center for Imaging Science, Rochester Institute of Technology, Rochester, NY, USA. His research interests include imaging spectroscopy (hyperspectral), light detection and ranging (lidar) applications in forestry, and precision agriculture.